

Displaced Ensemble variational assimilation method to incorporate microwave imager brightness temperatures into a cloud-resolving model

Kazumasa AONASHI * and Hisaki EITO

Meteorological Research Institute, Nagamine 1-1, Tsukuba, Ibaraki, 305-0052, Japan – ([aonashi and heito](mailto:aonashi.and.heitou@mri-jma.go.jp))@mri-jma.go.jp)

KEY WORDS: Displacement error correction, Ensemble assimilation method, microwave imager, cloud-resolving model

ABSTRACT:

We developed a data assimilation method that incorporates the microwave imager (MWI) brightness temperatures (TBs) into the cloud-resolving model (CRM) developed by the Japan Meteorological Agency (JMANHM). This method consisted of a displacement error correction scheme and an Ensemble-based variational assimilation scheme. In the displacement error correction scheme, we obtained the optimum displacement that maximized the conditional probability of TB observation given the displaced CRM variables. In the assimilation scheme, we derived a cost function in the displaced Ensemble forecast error subspace. Then, we obtained the analyses of CRM variables by non-linear minimization of the cost function. We applied this method to assimilate TMI (TRMM Microwave Imager) low-frequency TBs (10, 19, and 21 GHz with vertical polarization) for a Typhoon case around Okinawa (9th June 2004). The results of the assimilation experiments showed that the assimilation of TMI TBs alleviated the large-scale displacement errors and improved the CRM forecasts.

1. INTRODUCTION

The goal of the present study is to develop a method to assimilate MWI TBs into CRMs. The assimilation requires the CRM forecast error covariance that shows distinct amplitude and scale differences between rainy and rain-free areas. To address the non-linearity of TBs and the flow-dependency of the error covariance, we adopted the Ensemble-based variational data assimilation (EnVA) method that has been proposed by Lorenc (2003) and Zupanski (2005).

The Ensemble-based assimilation methods are based on the presupposition that the Ensemble forecasts have enough spread to include differences between the observation and the Ensemble mean. Hence, these methods can give erroneous analysis for observed rain areas without forecasted rain where the presupposition is not satisfied. However, there often exist such areas due to large-scale displacement errors of rainy areas between the MWI observation and the CRM forecasts (Aonashi 2009).

In order to solve this problem, we propose the EnVA that uses Ensemble forecast error covariance with displacement error correction. Based on this idea, we developed a data assimilation method that incorporates the MWI TBs into the CRM developed by the Japan Meteorological Agency (JMANHM). This method consisted of the displacement error correction (DEC) scheme and the EnVA scheme. In the DEC scheme, we obtained the optimum displacement that maximized the conditional probability of TB observation given the displaced CRM variables. In the EnVA scheme, we obtained the analyses of CRM variables by non-linear minimization of the cost function in the displaced Ensemble forecast error subspace. (The detail is described in Aonashi and Eito (2010).)

We applied this method to assimilate TMI (TRMM Microwave Imager) low-frequency TBs (10, 19, and 21 GHz with vertical polarization) for a Typhoon case around Okinawa (9th June 2004). We performed assimilation experiments to see the impact of the assimilation on the CRM analyses and forecasts.

2. DATA, CRM AND RTM USED

2.1 TMI TBs

TMI is a five-frequency, nine-channel, conical-scanning MWR that measures at 10.7, 19.7, 21.3, 37, and 85.5 GHz (hereafter referred to as 10, 19, 21, 37, and 85 GHz) with an incident angle of 52.8 degree. Each frequency has one vertical (V) and one horizontal (H) polarized channel, except for the water vapor absorption band, 21 GHz that only has vertical polarization channel. The swath width of TMI is limited to 760 km because of the low orbit altitude of TRMM (about 400 km). In the present study, we used TMI 1B11 version 6 as the MWR TB data.

2.2 CRM

We employed JMANHM with horizontal resolution of 5 km (Saito et al. 2006) that used a bulk microphysical scheme to predict explicitly 6 hydrometers (Ikawa and Saito 1991).

Using this CRM, we performed 100-member Ensemble forecasts that started with perturbed initial values. We made these initial perturbed values by adding perturbations with various horizontal and vertical scales to the routine analysis data (Houtekamer and Mitchell 1998).

2.3 RTM

We calculated the TBs by incorporating the outputs of the CRM Ensemble forecasts into the RTM program of Liu (2004). This program computed TBs for plane-parallel atmosphere by a four stream approximation. In the present study, all precipitation particles were assumed to be spherical, and absorption and scattering coefficients and phase functions were computed from the Mie theory.

Eito and Aonashi (2009) reported that the RTM-calculated TBs from JMANHM had good agreement with observations for low-frequency range (< 37 GHz), but that the calculated TBs showed significant biases due to the CRM model errors. Thus, we chose low-frequency TBs (10, 19, and 21 GHz) with vertical polarization as the input of the assimilation system.

3. ASSIMILATION METHOD

We introduced displacement error \vec{d} in addition to the CRM variables \vec{X} as the analysis values that the assimilation system should search for. Hence, the assimilation results in finding the optimum values \vec{X}^a, \vec{d}^a that maximize the conditional probability of \vec{X}, \vec{d} given the observed TBs (Y) and the first guess of \vec{X} (\vec{X}^f), $P(\vec{X}, \vec{d} | Y, \vec{X}^f)$. In the present study, we chose the mean of the Ensemble forecasts as \vec{X}^f .

The conditional probability $P(\vec{X}, \vec{d} | Y, \vec{X}^f)$ can be written as: $P(\vec{X}, \vec{d} | Y, \vec{X}^f) = P(\vec{d} | Y, \vec{X}^f)P(\vec{X} | \vec{d}, Y, \vec{X}^f)$. (1)

Thus, finding \vec{X}^a, \vec{d}^a is divided into the following 2 steps:

- 1) Find the optimum \vec{d}^a that maximizes $P(\vec{d} | Y, \vec{X}^f)$ (displacement error correction scheme);
- 2) Find the optimum \vec{X}^a that maximizes $P(\vec{X} | \vec{d}^a, Y, \vec{X}^f)$ (Ensemble-based variational assimilation scheme).

3.1 Displacement error correction scheme

3.1.1 Conditional probability of the displacement error: We derived the conditional probability of the displacement error in the following way. First, we transformed $P(\vec{d} | Y, \vec{X}^f)$ using the Bayes' theorem:

$$P(\vec{d} | Y, \vec{X}^f) = P(Y | \vec{d}, \vec{X}^f)P(\vec{d}, \vec{X}^f) / P(Y, \vec{X}^f). \quad (2)$$

Then, $P(Y | \vec{d}, \vec{X}^f)$ can be expressed as the conditional probability of Y given \vec{X}^f displaced with \vec{d} , $\vec{X}^f(\vec{d})$:

$$P(Y | \vec{d}, \vec{X}^f) = \exp\{-1/2(Y - H(\vec{X}^f(\vec{d})))' R^{-1}(Y - H(\vec{X}^f(\vec{d})))\}. \quad (3)$$

Assuming the mutual independency of \vec{d} , \vec{X}^f , and Y , we have:

$$P(\vec{d}, \vec{X}^f) / P(Y, \vec{X}^f) = P(\vec{d}) / P(Y). \quad (4)$$

We also assumed the Gaussian distribution of $P(\vec{d})$:

$$P(\vec{d}) = \exp\{-1/2(\vec{d}' E_d^{-1} \vec{d})\}, \quad (5)$$

where E_d is the covariance matrix of the displacement error. Substituting (3)-(5) into (2) yields:

$$P(\vec{d} | Y, \vec{X}^f) = \exp(-J_d) / P(Y), \text{ where } J_d = 1/2(Y - H(\vec{X}^f(\vec{d})))' R^{-1}(Y - H(\vec{X}^f(\vec{d}))) + 1/2(\vec{d}' E_d^{-1} \vec{d}) \quad (6)$$

3.1.2 Search for the optimum displacement: We derived the optimum displacement error \vec{d}^a by minimizing the cost

function J_d in the following way:

- 1) Transformation of \vec{d} into control variables in wave space.
- 2) Computation of gradient of the cost function in terms of the control variables.
- 3) Minimization of the cost function using the computed gradient.

For this minimization, we employed the variational assimilation techniques of Hoffman and Grassotti (1996).

3.2 Ensemble-based variational assimilation scheme

Following Lorenc (2003) and Zupanski (2005), we made a variational assimilation scheme that used Ensemble forecast error $\vec{X}_i^f - \vec{X}^f$, where \vec{X}_i^f and \vec{X}^f denote the forecast of member i and the Ensemble mean, respectively.

3.2.1 Cost function in Ensemble forecast error subspace: We defined cost function for $\vec{X} - \vec{X}^f$, J_x as follows:

$$J_x = 1/2(\vec{X} - \vec{X}_f)' P_f^{-1}(\vec{X} - \vec{X}_f) + 1/2(Y - H(\vec{X}))' R^{-1}(Y - H(\vec{X})) \quad (7)$$

Following Lorenc (2003), we assumed that analysis error $\vec{X} - \vec{X}^f$ belonged to the subspace spanned by N -member Ensemble forecast error:

$$\vec{X} - \vec{X}^f = P_e^{f/2} \circ \Omega, \quad (8)$$

where $P_e^{f/2} = (1/\sqrt{N-1})[\vec{X}_1^f - \vec{X}^f, \vec{X}_2^f - \vec{X}^f, \dots, \vec{X}_N^f - \vec{X}^f]$, (9)

$\Omega = [\vec{w}_1, \vec{w}_2, \dots, \vec{w}_N]$, \vec{w}_i denotes the analysis increment of member i in the subspace, and \circ denotes the Schur product.

Then, we defined the forecast error covariance P_f by localizing the Ensemble forecast error covariance with a weighting function matrix S :

$$P^f = P_e^f \circ N_x^2 S^{-1}, \quad (10)$$

where N_x is the dimension of \vec{X}^f .

Using (8)-(10), we can rewrite J_x in terms of Ω :

$$J(\Omega) = 1/2 \text{trace}\{\Omega' S^{-1} \Omega\} + 1/2 \{H(\vec{X}(\Omega)) - Y\}' R^{-1} \{H(\vec{X}(\Omega)) - Y\} \quad (11)$$

3.2.2 Search for the optimum analysis increment: We derived the optimum analysis increment Ω_a by minimizing the cost function $J(\Omega)$ in the following way:

- 1) Eigenvalue decomposition of S : $S = UDU^t$ (12)
- 2) Transformation of Ω into control variables: $\chi_i(m) = 1/d_m \{U^t \Omega\}_i(m)$ (13)
- 3) Computation of gradient of the cost function in terms of the control variables.
- 4) Minimization of the cost function using the computed gradient.

Then, we calculated the optimum state of the Ensemble mean using Ω_a . We also approximated Ensemble analysis error covariance P_e^a to derive the optimum state of each Ensemble members, following Zupanski (2005).

4. RESULTS

We applied the above assimilation method (DEC and EnVA

schemes) to incorporate TMI low-frequency TBs (22 UTC 9th June 2004) for a Typhoon case around Okinawa. As the first guess for the assimilation, we used 100-member CRM Ensemble forecasts started at 15 UTC 9th June 2004.

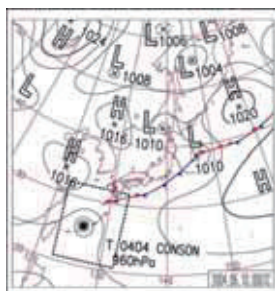
We performed the following assimilation experiments to examine the impact of the TMI TB assimilation on the CRM analysis: **(FG)** the experiment without assimilation that outputs the first guess, the mean of the Ensemble forecasts for 22 UTC 9th June 2004; **(DE)** the experiment that corrected the displacement errors of the first guess by the DEC scheme; **(CN)** the control experiment that applied the EnVA scheme to the output of DE; **(ND)** the experiment that applied the EnVA scheme to the first guess, without the DEC scheme. We also performed CRM forecasts started with the outputs of the above assimilation experiments to examine the impact of the TMI TB assimilation on the forecasts.

4.1 Meteorological case

Figure 1 shows the surface weather chart for 00 UTC 10th June 2004. At this time, Typhoon Conson (T0404) was marching northeastward over sea west of Okinawa. A stationary front was extended over sea south of Kyushu and Honshu.

Figure 2.a and b show TMI TB19v and Radar-AMeDAS hourly precipitation, (hereafter referred to as RAM), respectively, for 22 UTC 9th June 2004 within the dotted-line box in Fig. 1. Areas with heavy rain and high TB19v (Region A in Fig. 2.a) were located around and to the northeast of the Typhoon center (x in Fig. 2.a) over sea west of Okinawa. There also existed a feeder band with heavy rain and high TB19v areas (Region B in Fig. 2.a) to the southeast of the Typhoon center over sea south of Okinawa. Other rain bands with high TB19v (Region C in Fig. 2.a) were formed in the warm sector of the stationary front over sea east of Okinawa.

Fig. 1: The surface weather chart for 00 UTC 10th June 2004.



4.2 Assimilation results

Figure 3.a (b) shows TB19v calculated from the FG analysis (rainwater mixing ratio, qr , at a height of 930 m and the surface pressure of the FG analysis). Comparing with Fig. 2, we found that large-scale positional differences in rainy areas between the observation and the FG analysis. In particular, the FG analysis had no rainy or high TB19v areas around Region B. Around the Typhoon center (in Region C), rainy areas in the

FG analysis were displaced several tens kilometers northwest (north) from the observation.

Figure 4.a (b) shows the displacement errors derived by the DEC scheme and TB19v calculated from the DE analysis (qr at a height of 930 m and the surface pressure of the DE analysis). The displacement error correction was about 125 ~ 150 km southeast in Region B, 75 km southeast around the Typhoon center, and 75 km south in Region C. This correction made the calculated TB19v in Region A closer to the TMI observation, compared with the FG analysis. The correction also induced weak rainy areas in Regions B and C, and reduced the TB differences from the TMI observation.

Fig. 2: (a) TMI TB19v (in K); (b) RAM (in mm hr⁻¹) for 22 UTC 9th June 2004 within the dotted-line box in Fig. 2.

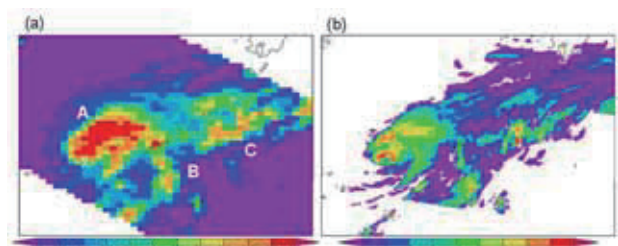


Fig. 3: (a) TB19v calculated from the FG analysis (in K); (b) the FG analysis of qr in g kg⁻¹ at a height of 930 m (shade) and the surface pressure in hPa (contours);

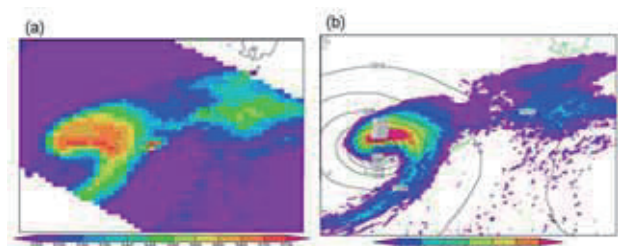


Fig. 4: (a) TB19v in K (contours) and the displacement error (arrows) calculated from the FG analysis; (b) Same as Fig.3 (b), but for the DE analysis.

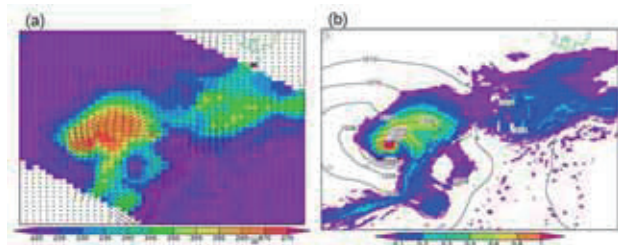


Figure 5.a (b) shows TB19v calculated from the CN analysis (qr at a height of 930 m and the surface pressure of the CN analysis). TB19v became higher and closer to the TMI observation than those of DE. Although qr increased in Regions B and C, qr was reduced by the assimilation of CN around the Typhoon center. This is because the sensitivity of TB19v to qr is negative due to scattering in heavy rain while the sensitivity is positive for weak rain range (precipitation rate

$< 10 \text{ mm hr}^{-1}$). The assimilation also amplified qr meso-scale patterns that was similar to the RAM precipitation distribution (Fig. 2.b).

Figure 6.a shows the CN analysis of RTW and w at a height of 4000 m. Figure 6.b is the vertical cross section of the CN analysis of RTW and w along L-L' in Fig. 6.a. The assimilation produced meso-scale humid areas (RTW $\sim 100\%$) in mid-troposphere and strengthened the updraft in upper- to mid-troposphere around Regions B and C.

Fig. 5: Same as Fig.3, but for the CN analysis.

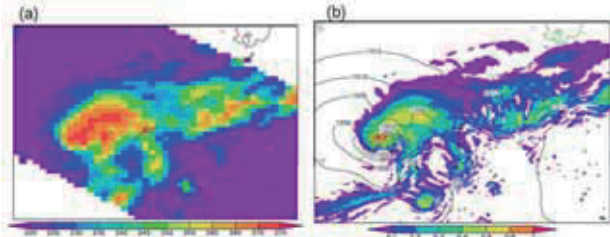


Fig. 6: (a) the CN analysis of RTW in % (contours) and w in m s^{-1} (shade) at a height of 4000 m. Areas with $|w| < 0.5 \text{ m s}^{-1}$ are masked; (b) the vertical cross section of the CN analysis of RTW in % (contours) and w in m s^{-1} (shade) along L-L' in Fig. 6.a. Areas with $|w| < 0.5 \text{ m s}^{-1}$ are masked. Areas with RTW $> 90\%$ are hatched.

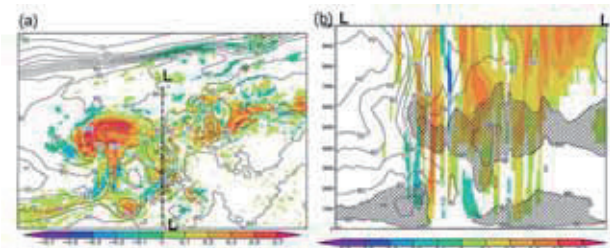


Figure 7.a (b) shows TB19v calculated from the ND analysis (qr at a height of 930 m and the surface pressure of the ND analysis). The ND analysis gave TB19v comparable with the observation in Regions A and C, In Region B, however, TB19v from ND was much lower than the observation and that from CN. In addition, the ND analysis of qr was noisier compared to the CN analysis, in particular around Regions B and C.

Figure 8.a shows the ND analysis of RTW and w at a height of 4000 m. Figure 8.b is the vertical cross section of the ND analysis of RTW and w along L-L' in Fig. 6.a. The assimilation of ND produced thick humid layers below 4 km and stronger updraft than CN in mid- to upper-troposphere around Regions B and C. Because the layers above 4 km were drier than the CN analysis, the ND analysis is more unstable about the moist convection than the CN analysis there. On the other hand, in Region D in Fig. 8.a to the west of the Typhoon center, the ND assimilation reduced RTW below 50% and produced downdraft stronger than 1.0 m s^{-1} in mid-troposphere, corresponding with large depression of TMI TBs from the FG calculation.

Fig. 7: Same as Fig.3, but for the ND analysis.

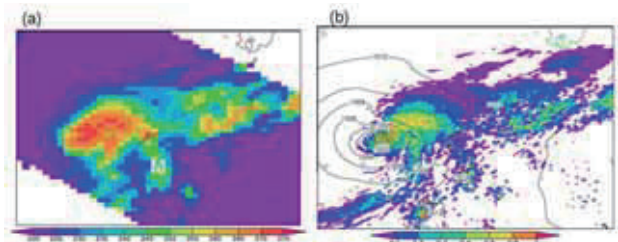


Fig. 8: Same as Fig.6, but for the ND analysis.

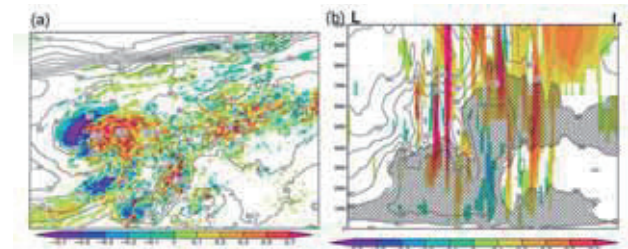
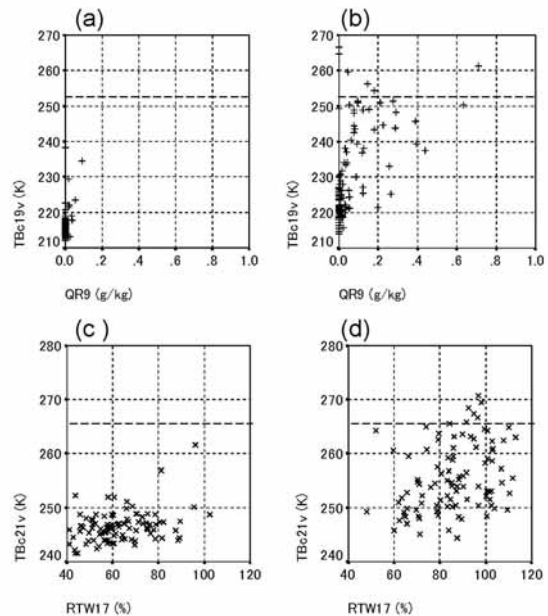


Fig. 9: (a) The scatter diagram of the first guess Ensemble at Point M between qr at a height of 930 m and the calculated TB19v. Dashed line denotes the TMI observation (252.2 K); (b) Same as (a), but for the displacement-error-corrected Ensemble; (c) The scatter diagram of the first guess Ensemble at Point M between RTW at a height of 4000 m and the calculated TB21v. Dashed line denotes the TMI observation (265.3 K); (d) Same as (c), but for the displacement-error-corrected Ensemble.



The above analysis differences between ND and CN arose from the difference that the assimilation of ND used the first guess Ensemble while the displacement-error-corrected Ensemble was adopted in CN. Hence, we compared the above 2 Ensembles (at Point M in Fig. 7.a) in terms of relationship

between CRM variables and calculated TBs.

Figure 9.a (b) shows the scatter diagram of the first guess Ensemble (the displacement-error-corrected Ensemble) at Point M between qr at a height of 930 m and the calculated TB19v. In the first guess Ensemble, no members had TB19v comparable with the observation (252.2 K). On the other hand, more than ten members had TB19v comparable with the observation in the displacement-error-corrected Ensemble. We consider that the lack of the comparable sample in the first guess caused the noise of the ND analysis, and that the CN analysis was stabilized by the members with the comparable TBs.

Figure 9.c (d) shows the scatter diagram of the first guess Ensemble (the displacement-error-corrected Ensemble) at Point M between RTW at a height of 4000 m and the calculated TB21v. In the first guess Ensemble, most members had RTW below 80%, and TB21v was not sensitive to RTW below 100%. On the other hand, in the displacement-error-corrected Ensemble, more than 30 members were humid (RTW \geq 100%), and TB21v had correlation with RTW above 60%. We consider that these differences in humid sample numbers and the TB sensitivity made ND analysis drier than CN analysis in the mid-troposphere.

4.3 Impact on CRM forecasts

We performed CRM forecasts that started with the FG, DE, CN, and ND analyses at 22 UTC 9th June 2004 in order to see the impact. (In these forecasts, we adopt the same CRM settings with those used for the Ensemble forecast, except for the initial values.)

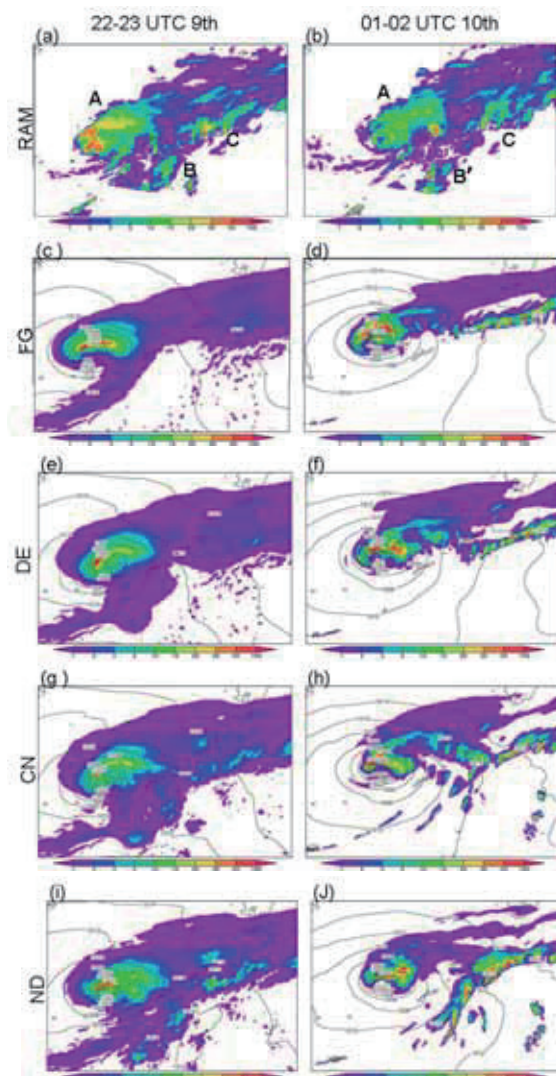
Figure 10 shows hourly precipitation of RAM and these CRM forecasts for 22-23 UTC 9th and 01-02 UTC 10th June 2004. Heavy rain was observed around and to the northeast of the Typhoon center (Region A in Fig. 10.a and Region A' in Fig. 10.b). Heavy rain was also found around the feeder band (Regions B and B') and in the warm sector of the stationary front (Regions C and C').

The FG forecast produced rainy areas around the Typhoon center, the feeder band, and the warm sector for the first one hour (Fig. 10.c). The forecasted areas, however, had large-scale displacement errors, compared to Regions A, B, and C. In the FG forecast after 23 UTC 9th, the rainy areas around the feeder band disappeared (Fig. 10.d). While rain was maintained around the Typhoon center and the warm sector, the large-scale displacement errors also remained.

The DE forecast produced weak rain in Regions B and C for the first one hour (Fig. 10.e). In addition, DE forecasted the Typhoon center and rain distribution in Region A closer to RAM than the FG forecast. In the DE forecast after 23 UTC 9th, heavy rain areas formed in Region C to the south of the FG forecasted areas (Fig. 10.f). This reduced the displacement errors in this region. The DE forecast, however, did not

maintain the rainy areas in the feeder band. The DE forecast also had displacement errors in Region A', mainly because the forecasted Typhoon center was dislocated northwestward from RAM and became closer to the FG forecast. This suggests that the displacement error correction of Typhoons needs to change flow patterns in wide range as well as around their centers.

Fig. 10: (a) RAM (in mm hr⁻¹) for 22-23 UTC 9th June 2004 within the dotted-line box in Fig. 2; (b) Same as (a), but for 01-02 UTC 10th June 2004; (c) The FG forecast of hourly precipitation in mm hr⁻¹ (shade) for 22-23 UTC 9th June 2004 and the surface pressure in hPa (contours) for 23 UTC 9th June 2004; (d) Same as (c), but for 01-02 UTC 10th June 2004; (e) Same as (c), but for the DE forecast; (f) Same as (d), but for the DE forecast; (g) Same as (c), but for the CN forecast; (h) Same as (d), but for the CN forecast; (i) Same as (c), but for the ND forecast; (j) Same as (d), but for the ND forecast.



The CN forecast produced heavier rain in Regions B and C than the DE forecast for the first one hour (Fig. 10.g). This made the CN precipitation patterns closer to RAM compared to the DE forecast in these regions. The CN forecast also maintained small-scale rainy areas around the feeder band after 23 UTC 9th, while their rain intensity and area coverage were

smaller than RAM (Fig. 10.h). This suggests that both moistening by DEC and strong updraft by EnVA were essential for the maintenance of the feeder band rainy areas. In Regions A' and C', the CN forecast had similar rain patterns to the DE forecast.

The ND forecast produced heavier rain in Regions B and C than the DE forecast for the first one hour (Fig. 10. i). Compared to the CN forecast, the forecasted rain covered wider areas to the west and south of the Typhoon center where FG forecasted the heavy rain. The ND forecast produced heavy rain bands around the feeder band and the warm sector after 23 UTC 9th, which overestimated the RAM rain intensity (Fig. 10.j). We consider that this overestimation was caused by the excessive moist convective instability and the updraft given by the ND analysis in these regions. On the contrary, the ND forecast had weaker rain than RAM and the CN forecast in Region A', downwind of Region B'. These errors made the ND forecast inferior to the CN forecast in terms of large-scale rain patterns.

The above results indicate that, among the 4 experiments, the CN analysis gave the best precipitation forecast, compared to RAM.

5. CONCLUSIONS

There often exist large-scale displacement errors of rainy areas when we assimilate the MWI TBs into the CRM. In order to address this problem, we propose the Ensemble-based assimilation that uses Ensemble forecast error covariance with displacement error correction. Based on this idea, we developed a data assimilation method that incorporates the MWI TBs into the CRM (JMANHM). This method consisted of the DEC scheme and the EnVA scheme. In the DEC scheme, we obtained the optimum displacement that maximized the conditional probability of TB observation given the displaced CRM variables. In the EnVA scheme, we derived a cost function in the displaced Ensemble forecast error subspace. Then, we obtained the analyses of CRM variables by non-linear minimization of the cost function.

We applied this method to assimilate TMI low-frequency TBs for the Typhoon case around Okinawa (9th June 2004). The results show that the assimilation of TMI TBs alleviated the large-scale displacement errors and improved the CRM forecasts. The DEC scheme (the EnVA scheme) contributed to this alleviation by moistening the mid- to lower-troposphere (by inducing updraft in the mid-troposphere in the observed rain areas). The DEC scheme also increased the number of Ensemble members with calculated TBs comparable to the observation, and reduced the noise in the analysis of the EnVA scheme.

6. REFERENCES

Aonashi, K., 2009: Neighboring Ensemble method for assimilation of microwave brightness temperatures into a cloud-resolving model, Proceedings of the 95th Conference of Japan Meteorological Society, 172. (in Japanese).

Aonashi, K. and H. Eito, 2010: Displaced Ensemble variational assimilation method to incorporate microwave imager brightness temperatures into a cloud-resolving model, *submitted to J. Meteor. Soc. Japan*.

Eito, H. and K. Aonashi, 2009: Verification of hydrometeor properties simulated by a cloud-resolving model using a passive microwave satellite and ground-based radar observations for a rainfall system associated with the Baiu front, *J. Meteor. Soc. Japan*, 87A, 425–446, 2009.

Hoffman, R.N., and C. Grassotti, 1996: A Technique for Assimilating SSM/I Observations of Marine Atmospheric Storms: Tests with ECMWF Analyses. *J. Appl. Meteor.*, **35**, 1177–1188.

Houtekamer, P.L., and H.L. Mitchell, 1998: Data Assimilation Using an Ensemble Kalman Filter Technique. *Mon. Wea. Rev.*, **126**, 796–811.

Ikawa, M. and K. Saito, 1991: Description of a nonhydrostatic model developed at the Forecast Research Department of the MRI. *Tech. Rep. MRI*, **28**, 238 pp.

Liu, G., 2004: Approximation of Single Scattering Properties of Ice and Snow Particles for High Microwave Frequencies. *J. Atmos. Sci.*, **61**, 2441–2456.

Lorenc, A.C. 2003: The potential of the ensemble Kalman filter for NWP - a comparison with 4D-Var. *Q. J. R. Meteorol. Soc.*, **129**, 3183–3203.

Saito, K., T. Fujita, Y. Yamada, J. Ishida, Y. Kumagai, K. Aranami, S. Ohmori, R. Nagasawa, S. Kumagai, C. Muroi, T. Kato, H. Eito, and Y. Yamazaki, 2006 : The operational JMA nonhydrostatic model. *Mon. Wea. Rev.*, **134**, 1266–1298.

Zupanski M. 2005. Maximum Likelihood Ensemble Filter: Theoretical aspects. *Mon. Weather Rev.* **133**: 1710-1726.

7. ACKNOWLEDGEMENTS

The present study is partially supported by Japan Aerospace Exploration Agency (JAXA) under the Global Precipitation Measuring mission (GPM) research grant. The initial and boundary data for JMANHM were provided by the numerical prediction division, JMA. TMI data were provided by the Goddard Space Flight Center, NASA. The RTM used in the present study was provided by Dr. Guosheng Liu, Florida State University.